A thermal coupling methodology of an arc-plasma and weld pool, a TIG welding model

Christopher Nahed, Stephane Gounand, Pierre Verpeaux

A coupling methodology of an arc-plasma and weld pool, a TIG welding model

Dr. Christopher Nahed, Eng. Stéphane Gounand, Eng. Pierre Verpeaux
Université Paris-Saclay, CEA,
Service d'études Mécaniques et Thermiques,
91191, Gif-sur-Yvette, France.

Abstract

A focus on a novel conjugate heat transfer method used to couple the arc-plasma and workpiece (weld pool included) domains in a unified Tungsten Inert Gas welding model is presented in this paper. The method uses a non-associated relation to implement an asymmetric thermal constraint when coupling the arc and workpiece domains. The method is shown to be conservative and robust. The algorithm is used in a unified 3D TIG welding model with displacement effects. The promising simulation results are compared to experimental work from the literature.

1 Introduction

The use of arc plasmas as heat sources has become widespread in the manufacturing community in recent decades. In fact, arc-plasmas are used in applications ranging from (but not limited to) high temperature furnaces in steel making, metal welding and joining to additive manufacturing. The popularity of arc-plasmas in the metal manufacturing community is due to their duel role as a shielding fluid, that serves to protect the hot metals from oxidation, and as a high temperature heat source [1], [2], [3], [4]. The importance of arc based manufacturing techniques has thus motivated the mathematical modelling of the complex physical interactions that occur between the arc-plasmas and the melt pools generated. Moreover, the rise in computational power in recent decades has motivated an ever-increasing complexity of the physical models [1], [4], [9], [10], [12].

Regarding welding applications, Tungsten Inert Gas (TIG) welding is largely one of the reference manufacturing techniques in the nuclear industry; thus the French *Commissariat à l'Énergie Atomique* (CEA) strongly invests in its mastery [1], [4]. Thus, the need to master the technique motivates the efforts put into the multiphysics modelling, the numerical simulation of TIG welding and its effects on the target metallic workpieces. Moreover, the ultimate goal of the multiphysics modelling of TIG welding is to develop a fully predictive computational model that uses typical welding parameters (arc-height, inlet current, materials etc…) to accurately predict the thermo-mechanical responses of the welded workpiece. To achieve the intended accuracy, the multiphysics modelling of TIG welding is centred on augmenting the physical representativity of the process model (the accurate modelling of the TIG process itself). To this end, a focus on the magneto-thermo-hydrodynamic (MTH) modelling of the arc-plasma and weld pool interactions is necessary. The basis of MTH modelling is mathematically describing the interactions between the electro-dynamically forced TIG arcs, the thermo-hydraulics of the molten metal (filler metal and/or target workpiece)

and the interfacial phenomena between the conjugate cathode, arc, liquid and solid metal. Thus, on a fundamental level, MTH modelling of the TIG process serves to improve the predictability of the generated thermal fields of the workpiece during welding. The accurately predicted thermal fields could then be used to feed mechanical and/or metallurgical models [1], [7], [8].

In this paper, we focus on treating the interface thermo-hydraulics of the conjugate arc and pool subdomains, where particular numerical difficulties are encountered. The difficulties are largely due to both the numerical stability of data exchange and the non-linear heat and momentum transfer phenomena that occur at the plasma-pool interface [1], [5], [6]. To this end, we present a robust and novel interface coupling method that allows for a conservative conjugate heat transfer as shown by a 3D simulation of a moving TIG weld configuration (with no filler metal). The novel approach uses an asymmetric thermal constraint to implement a conservative quasi-monolithic algorithm that couples the arc-plasma and weld workpiece domains. The mathematical details show that by using the novel algorithm the heat transfer at the interface is conserved, but thermal continuity is only achieved at algorithm convergence. Certain simulation results are then compared to an experimental case as performed by Koudadge [9].

The paper begins by presenting the governing equations of the physics model, then the weak formulation and the numerical implementation of the model are presented, then the geometry and problem configuration are presented, then some results are discussed.

2 Governing equations

In this section, we present the governing equations of our multiphysics model. The differential equations used to define the multiphysics model capture the various dominant phenomena found in TIG welding. The multiphysics model is constructed based on a TIG configuration as schematised in Figure 1. The model is based on the dominant electrodynamic laws, mass, momentum and energy conservation laws, under local thermodynamic equilibrium (LTE) assumptions in the entire domain $\Omega_{tot} = \Omega_{cat} \cup \Omega_{pla} \cup \Omega_{ano}$ [1], [2], [4]. The chosen arc and workpiece models are to be compatible with both conjugate heat transfer and phase change phenomena, while also allowing for the capture of the deformable arc-pool interface dynamics. We note that the model used in this paper is a stationary one that models the TIG system at long time scales [1], [4].

For brevity, only the heat transfer model used in this study is presented here; and so the interested reader is referred to the full physics model as it was described in detail in Nahed's dissertation [1].

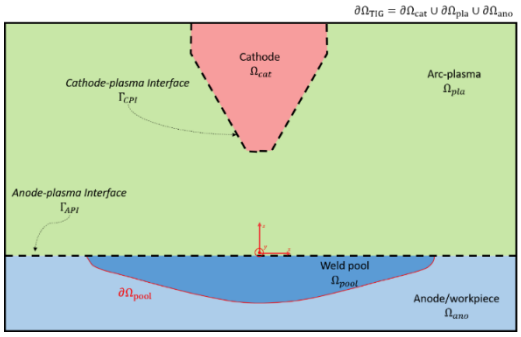

Figure 1: Schematic of the TIG system [1]

2.1 Energy conservation model

The TIG welding system is made up of three bodies that transform electrical energy into heat and that transfer the generated heat to the workpiece, which melts to form the liquid weld pool. The cathode, arc-plasma and the workpiece subdomains are simultaneously subject to electro-thermal, heat transport and phase change phenomena. Thus, to effectively capture the range of thermal effects in the TIG system, the energy conservation law must be modelled in a manner compatible with both conjugate heat transfer and phase change phenomena. To this end, energy conservation in both the cathode and arc-plasma are modelled using the temperature variable as the primary unknown variable, while energy conservation in the workpiece is modelled using the enthalpy variable. The mixed variable method is used because the temperature based models allow for a simpler expression of the electro-thermal phenomena in the cathode and arc-plasma, while the enthalpy based model is adapted for the capture of phase change effects (solid to liquid) in the workpiece.

2.1.1 Temperature based energy conservation model

The cathode and arc-plasma interact electro-thermally to transmit and transform electrical energy into thermal energy useful for TIG welding. The cathode is modelled as a solid, and the arc-plasma is modelled to maintain LTE. However, for the sake of brevity, the presented thermal analysis is centred around the anode-plasma interface Γ_{API} (see Figure 1). For details regarding the hypotheses and complete model, the interested reader is referred to [1], [4].

Arc-plasma subdomain

The energy conservation law in the arc-plasma subdomain is modelled using the following equation [4]:

$$\rho c_p \boldsymbol{u} \cdot \nabla T = \nabla \cdot (\lambda \nabla T) + s_{Joule} - s_{Ray,pla}$$

where the mass density ρ, the specific heat c_p, and the thermal conductivity λ of argon are detailed in appendix A in Nahed [1]. The arc-plasma velocity field is represented as $\boldsymbol{u}$. Heat generation in the arc-plasma is modelled by the Joule Effect, as given by:

$$s_{Joule} = (\sigma^* \nabla\phi) \cdot \nabla\phi$$

where σ^* is the electrical conductivity and ϕ the electric potential (see Ch. 2 in [1] for details). As for the total radiated heat, it is adapted from Lago et al. [10] and is modelled in the following manner:

$$s_{Ray,pla} = 4\pi\epsilon_n$$

where ϵ_n is the total argon plasma emissivity term and is given as a function of temperature in appendix A in Nahed [1].

2.1.2 Enthalpy based energy conservation model

The heat transported by the arc-plasma melts the weld zone of the workpiece, inducing phase change over the course of a welding operation. The phase change process is generally strongly temperature dependent and nonlinear in that the enthalpy of the studied material rises significantly over a small temperature range. For incompressible fluids, an isobaric enthalpy relation can be defined as:

$$h = \int_{T_{ref}}^{T} c_p \, dT$$

which applies for both the solid and liquid states of the workpiece [1]. The notion of using enthalpy as the unknown variable in place of the temperature is important when studying phase change because it masks the strongly nonlinear dependence of phase change onto temperature by acting as an integral quantity. This is evident when comparing the expression of enthalpy (for non-isothermal phase change) as a function of temperature, where the specific heat for a material undergoing fusion is:

$$c_p = \begin{cases} c_{p_s} & \text{for } T < T_s \\ L_f \sqrt{\dfrac{1}{2\pi(\Delta T_m/a)^2}} \exp\left(-\dfrac{(T-T_c)^2}{2(\Delta T_m/a)^2}\right) & \text{for } T_s \le T \le T_l \\ c_{p_l} & \text{for } T < T_s \end{cases}$$

where T_s and T_l are the solidus and liquidus temperatures of the material, L_f the latent heat of fusion, $T_m = T_l - T_s$ the mushy temperature range, $T_c = (T_l + T_s)/2$ the mushy centre temperature, and a a sharpness factor to be > 1. While the enthalpy of a material undergoing fusion is defined as:

$$h = \begin{cases} \displaystyle\int_{T_{ref}}^{T} c_{p_s} \, dT & \text{for } T < T_s \\ \displaystyle\int_{T_{ref}}^{T_s} c_{p_s} \, dT + L_f f_l & \text{for } T_s \le T \le T_l \\ \displaystyle\int_{T_{ref}}^{T_s} c_{p_s} \, dT + L_f + \int_{T_l}^{T} c_{p_l} \, dT & \text{for } T < T_s \end{cases}$$

where f_l is the liquid fraction defined as $f_l\,(T < T_s) = 0$, $f_l\,(T > T_l) = 1$, $f_l\,(T_s < T < T_l) = (T - T_s)/T_m$. The interested reader is referred to appendix B of [1] for details on the derivation of the enthalpy-specific heat-temperature relation. The enthalpy-temperature and specific heat-temperature relations are schematised in Figure 2, where the strong non-linearity of c_p is evident when compared to h. Thus, using the enthalpy variable instead of the temperature variable in the energy conservation model is better adapted at capturing phase change effects [1], [11]. The energy conservation model for the workpiece becomes:

$$\rho \boldsymbol{v} \cdot \nabla h = \nabla \cdot \left(\lambda \nabla \frac{h}{c_p^*} \right) + s_{Joule}$$

where ρ, $\boldsymbol{v}$, c_p^* and λ are the density, pool velocity, a specific heat averaged in the mushy zone and thermal conductivity of the weld pool, respectively. The material properties are presented in appendix A of [1]. Note that in the solid domain of the workpiece, $\boldsymbol{v} = \mathbf{V}_{\boldsymbol{displ}}$, the weld displacement velocity, w.r.t the laboratory reference frame.

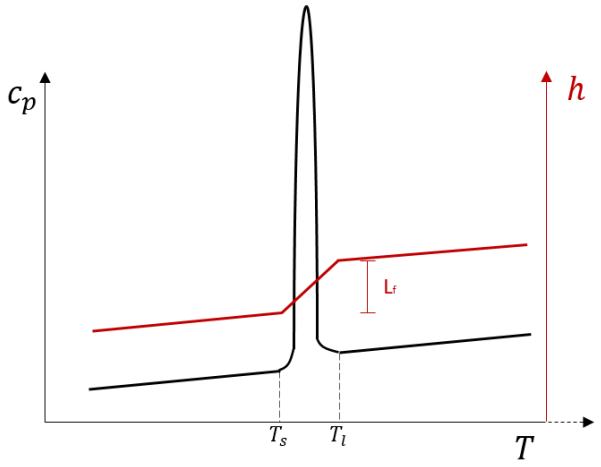

Figure 2. Superimposed plots of schematised the workpiece c_p and h. Not to scale [1].

2.1.3 Interfacial phenomena at the anode-plasma interface

We remind the reader that only the interfacial phenomena modelled at Γ_{API}(see Figure 1) are discussed here. The continuity of the temperature field across Γ_{API} is imposed following the LTE hypothesis, where the thermal continuity expressed using both the temperature and enthalpy variables becomes:

$$T_{\Gamma_{pla}} = T_{\Gamma_{ano}}$$

and

$$h_{\Gamma_{ano}} = c_p(T) dT_{\Gamma_{ano}}$$

thus

$$T_{\Gamma_{pla}} = \left[\int_{h_{ref}}^{h} \frac{1}{c_p(T)}\, dh\right]_{\Gamma_{\text{ano}}} + T_{ref} \tag{1}$$

where h_{ref} is an arbitrary reference enthalpy calculated at some T_{ref}. Next, the energy conservation condition at Γ_{API} is expressed as (see [1][4] for a formal derivation):

$$\begin{aligned}\left((\rho \boldsymbol{u} \cdot c_p T)_{pla} - (\rho \boldsymbol{v} \cdot h)_{ano}\right) \cdot \boldsymbol{n} \\ = \left((\lambda\, \nabla T)_{pla} - \left(\lambda\, \nabla h / c_p^*\right)_{ano}\right) \cdot \boldsymbol{n} + \sum_{inte.} s_{\Gamma_{\text{API}}}\end{aligned} \tag{2}$$

where $\boldsymbol{n}$ is the normal to the interface Γ_{API} and $s_{\Gamma_{API}}$ represents the different interfacial heat sources (see [1], [4] for details).

3 The numerical methodology

For brevity, the presented analysis is centred around the anode-plasma interface Γ_{API} and on the thermo-hydraulic coupling methodology used in this study. The full details of the developed numerical model can be found in Nahed and Brochard's theses [1], [4]. We begin with a brief description of the finite element spaces:

3.1 Finite element formulation

The variational form of the physics models are presented in the following. The space of test functions is defined as $\mathcal{V}$ for all functions $N(\boldsymbol{x}) \in \mathcal{V}(\boldsymbol{x} \in \Omega)$ that are sufficiently smooth and square integrable and null at all boundaries. The space $\mathcal{V}$ can thus be written as:

$$\mathcal{V} = \{N(\boldsymbol{x}) \mid \boldsymbol{x} \in \Omega, \mathrm{N}(\boldsymbol{x}) \in \mathcal{H}_0^1(\Omega), N(\boldsymbol{x}) = 0 \text{ on } \partial\Omega\,\}$$

furthermore, using the Galerkin approach, we define the space of interpolation functions $\mathcal{W}$ similarly as:

$$W = \{N^T(\boldsymbol{x}) \mid \boldsymbol{x} \in \Omega, \mathrm{N}^{\mathrm{T}}(\boldsymbol{x}) \in \mathcal{H}_0^1(\Omega), N^T(\boldsymbol{x}) = 0 \text{ on } \partial\Omega\,\}$$

where $N^T(\boldsymbol{x})$ is used to redefine the primary unknowns, as shown below:

$$T(\boldsymbol{x}) = N^T(\boldsymbol{x}) T_{nodes} + \mathcal{O}(\Delta x^{r+1})$$

where r is the order of the polynomial order of the interpolation function $N^T(\boldsymbol{x})$. For a more formal description of the Galerkin method, the interested reader is referred to Reddy [13].

3.2 Conjugate heat transfer coupling algorithm

The energy conservation model presented in section 2.1 is numerically solved in a quasi-monolithic manner. The temperature based model used for the cathode and arc domains is coupled in a novel but simple manner to the workpiece domain. In fact, the quasi-monolithic approach in this work implies a coupling that strongly imposes heat flux conservation across the Γ_{API} interface (see Figure 1) while weakly imposing thermal continuity across the interface [1].

3.2.1 Monolithic variational model

The weak variational forms of the residuals of the stationary energy conservation models of both the arc-plasma and the melting workpiece are expressed and detailed in the following, and are based on the work in Nahed, Nguyen and Brochard [1], [4], [12].The approach presented here is monolithic because no domain partitioning is implemented. For the heat transfer model in the arc-plasma subdomain Ω_{arc}, with T as the primal unknown[1]:

$$0 = R_T = \int \left(\rho c_p \boldsymbol{u} \cdot \nabla T\right)^{\mathrm{T}} \cdot (N)\, d\Omega_{arc} + \int (\lambda \nabla T)^{\mathrm{T}} \cdot (\nabla N)\, d\Omega_{arc} - \int ((\lambda \nabla T) \cdot \boldsymbol{n}) \cdot (N)\, d\Gamma_{plaapi} + \int s_{joule} \cdot (N)\, d\Omega_{arc} - \int s_{Ray,pla} \cdot (N)\, d\Omega_{arc} \tag{3}$$

where Γ_{plaapi} is the plasma side of the Γ_{API} subdomain. The heat transfer model in the workpiece subdomain Ω_{ano}, with h as the primal unknown:

$$0 = R_h = \int (\rho \boldsymbol{v} \cdot \nabla h)^{\mathrm{T}} \cdot (N)\, d\Omega_{ano} + \int \left(\lambda \nabla h / c_p^*\right)^{\mathrm{T}} \cdot (\nabla N)\, d\Omega_{ano} - \int ((\lambda \nabla h / c_p^*) \cdot \boldsymbol{n}) \cdot (N)\, d\Gamma_{anoapi} + \int s_{joule} \cdot (N)\, d\Omega_{ano} \tag{4}$$

where Γ_{anoapi} is the anode side of the Γ_{API} where $\Gamma_{API} = \Gamma_{plaapi} \cup \Gamma_{anoapi}$. To couple equations (3) and (4), they are summed and the resulting residual becomes:

[1] For the sake of simplicity, the boundary conditions (at $\partial\Omega$) are not detailed in the following residuals. However, the interfacial conditions (at Γ_{API}) are explicity detailed.

$$
\begin{aligned}
0 = R_{total} = & \int (\rho \boldsymbol{v} \cdot \nabla h)^{\mathrm{T}} \cdot (N)\, d\Omega_{ano} + \int \left(\lambda \nabla h / c_p^*\right)^{\mathrm{T}} \cdot (\nabla N)\, d\Omega_{ano} \\
& + \int \left(\rho c_p \boldsymbol{u} \cdot \nabla T\right)^{\mathrm{T}} \cdot (N)\, d\Omega_{arc} + \int (\lambda \nabla T)^{\mathrm{T}} \cdot (\nabla N)\, d\Omega_{arc} \\
& - \int s_{Ray,pla} \cdot (N)\, d\Omega_{arc} + \int s_{joule} \cdot (N)\, d\Omega_{total} \\
& - \int \left([(\lambda \nabla T) \cdot (N)]_{plaapi} - \left[\left(\lambda \nabla h / c_p^*\right) \cdot (N)\right]\right)_{anoapi} \cdot \boldsymbol{n}\ \ d\Gamma_{API}
\end{aligned}
\tag{5}
$$

where the last term on the right hand side of equation (5) corresponds to the weak form of equation (2). Equation (5) requires a closure condition at the Γ_{API} interface, and thus equation (1) is recalled in the following form:

$$
\int \left(T_{pla} - T_{ano}(h_{ano})\right) \left(\delta(\boldsymbol{x} - \boldsymbol{x}_{plaapi}) - \delta(\boldsymbol{x} - \boldsymbol{x}_{anoapi})\right)\, d\Gamma_{API} = 0 \tag{6}
$$

and where $\delta(\boldsymbol{x} - \boldsymbol{x}_{API})$ represents the Dirac Delta operator with $\boldsymbol{x}$ representing the parametrised coordinate vector. Equation (6) is used as a constraint to equation (5), thus equation (5) is appended and becomes:

$$
\begin{aligned}
0 = R_{total} = & \int (\rho \boldsymbol{v} \cdot \nabla h)^{\mathrm{T}} \cdot (N)\, d\Omega_{ano} + \int \left(\lambda \nabla h / c_p^*\right)^{\mathrm{T}} \cdot (\nabla N)\, d\Omega_{ano} \\
& + \int \left(\rho c_p \boldsymbol{u} \cdot \nabla T\right)^{\mathrm{T}} \cdot (N)\, d\Omega_{arc} + \int (\lambda \nabla T)^{\mathrm{T}} \cdot (\nabla N)\, d\Omega_{arc} \\
& - \int s_{Ray,pla} \cdot (N)\, d\Omega_{arc} + \int s_{joule} \cdot (N)\, d\Omega_{total} \\
& - \int \left([(\lambda \nabla T) \cdot (N)]_{plaapi} - \left[\left(\lambda \nabla h / c_p^*\right) \cdot (N)\right]\right)_{anoapi} \cdot \boldsymbol{n}\ \ d\Gamma_{API} \\
& - \int \beta \left(\delta(\boldsymbol{x} - \boldsymbol{x}_{plaapi}) - \delta(\boldsymbol{x} - \boldsymbol{x}_{anoapi})\right)\, d\Gamma_{API}
\end{aligned}
\tag{7}
$$

where β is a Lagrange multiplier to the imposed constraint expressed in equation (6). Thus, equations (6) and (7) make up the conjugate heat transfer model as it manifests in its monolithic variational form. To facilitate the numerical implementation of the closure interface conditions of equation (6), geometrically overlapping nodes are numerical generated along the meshed interface. This is schematised in Figure 3, where the overlapping nodes make up the interfacial nodes of the mesh, and lie along the Γ_{plaapi} and Γ_{anoapi}, which exist in the submeshes of their respective subdomains Ω_{pla} and Ω_{ano}. The Lagrange multiplier $\beta_{i,j}$, the arc-plasma temperature field T_i and the anode enthalpy field h_j are applied on their respective nodes along the overlapping node zone as seen in Figure 3.

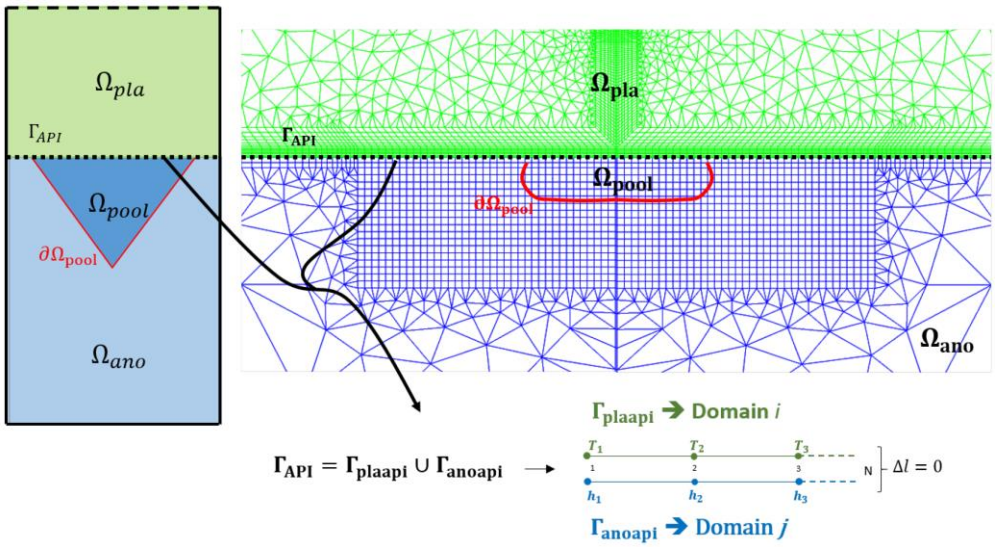

Figure 3. Simplified schematic of the arc Ω_{arc}, workpiece Ω_{ano} and anode-plasma interface Γ_{API} subdomains/

3.2.2 Quasi-monolithic algorithm

3.2.2.1 Linearised variational form

The two equation monolithic thermal system, equations (6) and (7), are both non-linear and of expressed with two variables (T and h). Therefore, before system assembly and resolution, the two equations are linearised by an approximate Newton-Raphson algorithm (see [1] for details). After linearising and applying a change of variable (from $T_{ano} \rightarrow h_{ano}$), equation (6) becomes:

$$\int \left(T_{pla} - \frac{h_{ano}}{c_p^*(T_{ref})}\right)\left(\delta(\boldsymbol{x} - \boldsymbol{x}_{plaapi}) - \delta(\boldsymbol{x} - \boldsymbol{x}_{anoapi})\right) d\Gamma_{API} = T_{ref} - \frac{h_{ref}}{c_p^*(T_{ref})} + \mathcal{O}(\delta T^2) \tag{8}$$

for an arbitrary reference temperature T_{ref} and enthalpy h_{ref} along Γ_{plaapi} and Γ_{anoapi}, respectively; where $\mathcal{O}(\delta T)$ represents higher order terms. The Jacobian (or tangent matrix) to the residual in equation (7) becomes (boundary condition contributions are omitted for simplicity):

$$
\begin{aligned}
[J]_{total} &= \underbrace{\left[\frac{\{R\}_{total}}{\{T\}}\right]}_{\mathbb{T}_{TT}} + \underbrace{\left[\frac{\{R\}_{total}}{\{h\}}\right]}_{\mathbb{T}_{hh}} + \underbrace{\left[\frac{\{R\}_{total}}{\{\beta\}}\right]}_{\mathbb{I}_{dual}} \\
&= \underbrace{\int (\lambda\, \nabla N)^{\mathrm{T}} \cdot (\nabla N)\, d\Omega_{arc} + \int \left(\rho c_p \boldsymbol{u} \cdot \nabla N\right)^{\mathrm{T}} \cdot N\, d\Omega_{arc}}_{\mathbb{T}_{TT}} \\
&+ \underbrace{\int \left(\frac{\lambda}{c_p^*} \nabla N\right)^{\mathrm{T}} \cdot (\nabla N)\, d\Omega_{ano} + \int (\rho \boldsymbol{v} \cdot \nabla N)^{\mathrm{T}} \cdot N\, d\Omega_{ano}}_{\mathbb{T}_{hh}} \\
&+ \underbrace{\int \left(\delta(\boldsymbol{x} - \boldsymbol{x}_{plaapi}) - \delta(\boldsymbol{x} - \boldsymbol{x}_{anoapi})\right) d\Gamma_{API}}_{\mathbb{I}_{dual}}
\end{aligned}
\tag{9}
$$

where $[J]_{total}$ is the total thermal Jacobian, $[\mathbb{T}_{TT}]$ the tangent matrix contribution associated to the temperature based residual, $[\mathbb{T}_{hh}]$ the tangent matrix contribution associated to the enthalpy based residual, and $[\mathbb{I}_{dual}]$ the dual contribution of the Lagrange multiplier β, as seen in column 3 of linear system (10).

3.2.2.2 *Linear system with asymmetric constraints*

Assembling equations (8), (9), and (7) in an iterative linearised system (in a manner that respects the Newton-Raphson algorithm), the system is expressed as:

$$
\begin{pmatrix} \mathbb{T}_{TT} & 0 & 1_i \\ 0 & \mathbb{T}_{hh} & -1_j \\ 1_i & -1_j/c_{p_j}^* & 0 \end{pmatrix}^{k-1} \begin{bmatrix} \delta T \\ \delta h \\ \beta_{i,j} \end{bmatrix}^{k} = - \begin{bmatrix} R_T \\ R_h \\ \mathcal{O}(\delta T^2) \approx 0 \end{bmatrix}^{k-1} \tag{10}
$$

where $[\mathbb{T}_{TT}]^{k-1}$ and $[\mathbb{T}_{hh}]^{k-1}$ represent the temperature and enthalpy tangent matrices, respectively, and $\{\delta T, \delta h\}^{k-1} = \{T, h\}^{k} - \{T, h\}^{k-1}$; where linear system (3) is to be solved for $k \to \mathcal{K}$ iterations until $\{R_T, R_h\}^{k-1} \approx 0$. The Lagrange multiplier $\beta_{i,j}^{k}$ at every geometrically overlapping node (see Figure 3) is equivalent to:

$$
\beta_{i,j}^{k} = \int \left([(\lambda \nabla T) \cdot (N)] \cdot \boldsymbol{n}\right)^{k} d\Gamma_i - \int \left(\left[\left(\lambda \nabla h / c_p^*\right) \cdot (N)\right] \cdot \boldsymbol{n}\right)^{k} d\Gamma_j \tag{11}
$$

where use of the linearised constraint from equation (8) in linear system (10) strongly couples (monolithically) the temperature model of the arc-plasma to the enthalpy model of the workpiece/anode [5], [6]. However, although the now

asymmetric constraint from equation (8) allows for a mixed variable coupling, it does not ensure thermal continuity at the Γ_{API} interface as imposed by equation (1). Rather the asymmetric constraint weakly imposes thermal continuity; thus, the constraint reaches thermal continuity only as the algorithm converges when $\{R_T, R_h\}^{k-1} \approx 0$. Furthermore, at every global iteration k, the enthalpy field calculated in the anode is used to calculate the temperature field associated to it. The inverse relation to $h = \int_{T_{ref}}^{T} c_p \, dT$ is used to this end, by simply using the inverse of the $h - T$ relations as extracted from the thermophysical data set used in Nahed (see appendix A) [1]. Using the calculated enthalpy fields and the $h - T$ relation, schematised by Figure 4, simple interpolation is used to find $T_{\Omega_{ano}}$. This methodology allows for the algorithm to use the fixed mesh at iteration k to identify the pool solidus and liquidus boundaries. The pool domain is then used to solve the momentum and mass conservation equations in the pool subdomain (whose numerical algorithm is detailed in [1]).

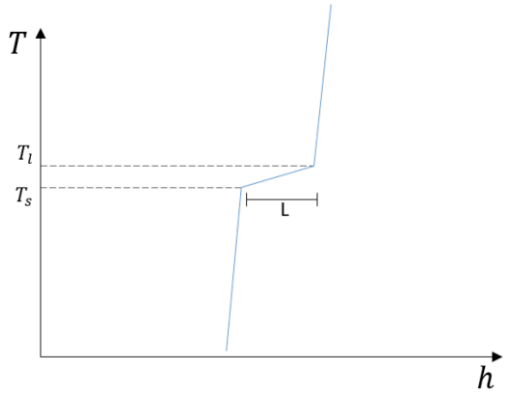

Figure 4. Typical temperature-enthalpy relation of a non-isothermal phase change process

3.2.2.3 A note on the stability of the interfacial asymmetric constraint

Although the asymmetric constraint approach is a specific case to the non-associated relation approach used by Verpeaux et al. [14], the asymmetric constraint approach conserves the interfacial heat flux because it is based on a minimisation problem [15]. Thus, the author hypothesises that the conservative property of the asymmetric constraint approach confirms the stability of the quasi-monolithic coupling between the two domains (Ω_{arc} and Ω_{ano}). However, the change of variable and the linearisation of the constraint, applied between equations (6) and (8), are what render the thermal continuity condition as weakly imposed. Furthermore, although a detailed theoretical analysis of the expected stability of the quasi-monolithic approach is out of the scope of this text, a sample axisymmetric TIG Spot simulation is performed with this algorithm. The welding parameters of the simulated configuration are, an electric intensity of I = 75 A for a thoriated tungsten cathode, an argon arc and a 316L steel. As seen in Figure 6 (a) the convergence of the temperature profiles (at ≈ 2000 K) at the Γ_{plaapi} and Γ_{anoapi} zones is achieved after only k ≈ 50 global iterations. This indicates that the temperature continuity condition of perfect thermal contact is rapidly approached, see equation (1). Furthermore, the global algorithm convergence plot is presented in Figure 6 (b), where all primal fields show a convergent trend. Thus, the reader is provided with a

preliminary proof of robustness of the quasi-monolithic approach presented in this study. A rigourous analysis of the asymmetric constraints in particular and the non-associated methods in general is the authors' current subject of study, to be presented in a future paper.

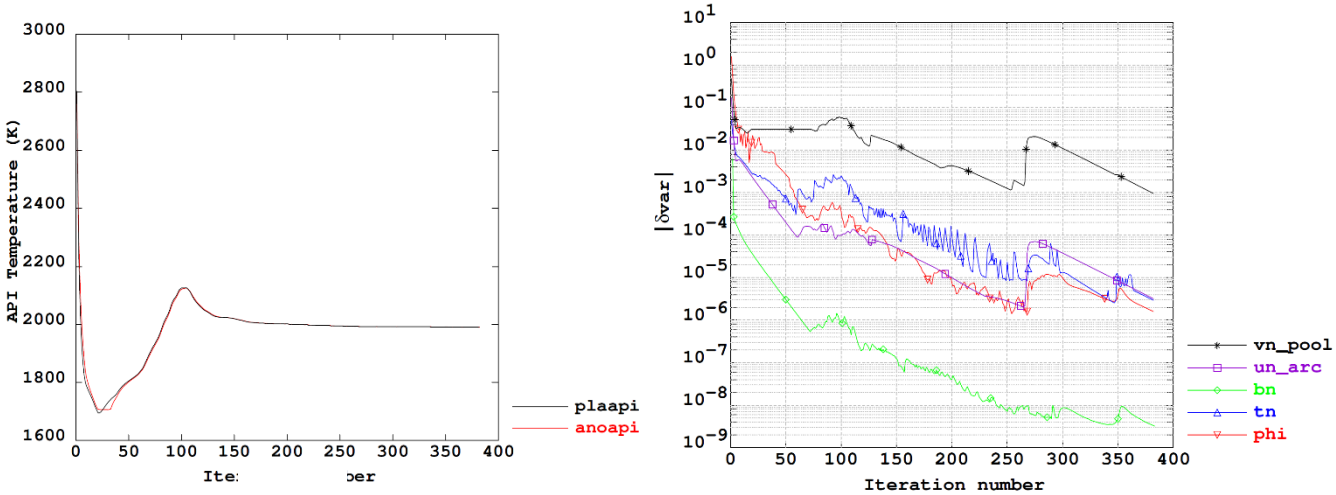

(a) (b)

Figure 5. a) Maximum temperature at Γ_{plaapi} (black plot) and at Γ_{anoapi} (red plot) interfaces as functions of iteration number. (b) Convergence plot of all variables of sample simulation

4 A 3D TIG welding configuration

4.1 Simulation setup

The brief results presented in this section are based on the simulations performed in the author's previous work, and the interested reader is to consult the manuscript in [1] for a detailed discussion of the 3D study. The 3D mesh, as shown in Figure 6, contains the cathode domain in red, the arc-plasma domain in green and the anode/workpiece domain in blue. The simulation presented is based on an experimental case taken from Koudadge [9], and has the following welding parameters:

$$\text{Experimental parameters} \longrightarrow \begin{cases} I_{arc} = 200 \text{ A} \\ H_{arc} = 3 \text{ mm} \\ \alpha = 20^{\circ} \\ r_{int} = \text{not specified} \\ c_S = 10 \text{ ppm} \\ H_{ano} = 18 \text{ mm} \\ \mathbf{V}_{displ} = 30 \text{ cm} \cdot \text{min}^{-1} \\ \text{Workpiece material} \rightarrow 304\text{L} \end{cases}$$

which are used to initialise the model before running the simulation. The temperature field of the global domain is calculated to be continuous across the

arc-plasma and workpiece domains, as is represented by the black isocontours, see Figure 7. The continuity of the temperature field implies that the energy

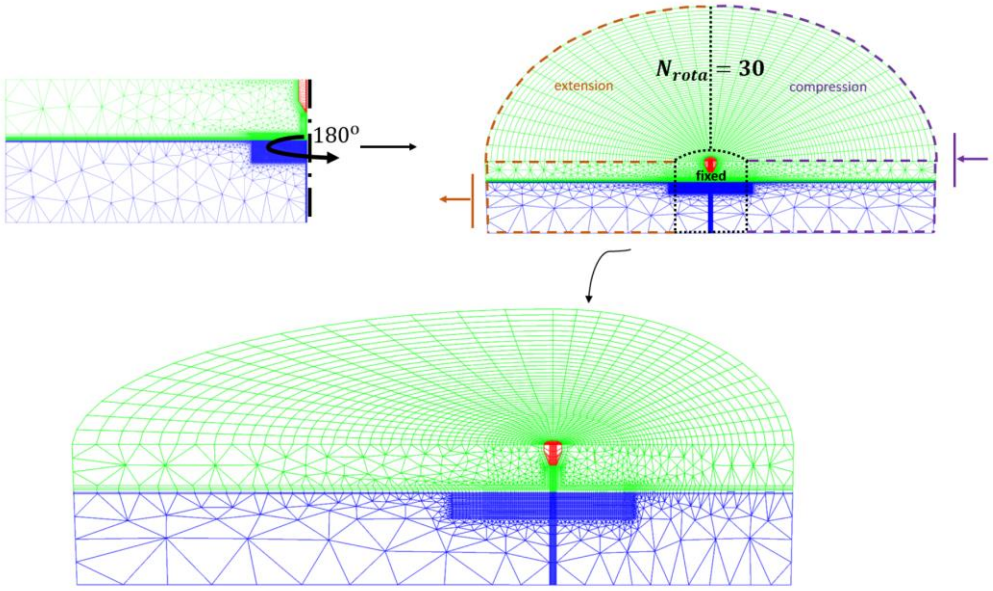

Figure 6. Mesh generation of 3D weld displacement model.

conservation laws are respected by the quasi-monolithic coupling algorithm implemented with asymmetric constraints (see section 3). This indicates that the algorithm is robust and generally applicable to 3D welding configurations. Furthermore, the temperature field of the arc-plasma displays an asymmetry in its interaction with the workpiece and this indicates the importance of modelling the arc-plasma in 3D. The full 3D model as it was solved with the numerical algorithms presented in this paper and in Nahed [1], shows promising results because of the similarity between the simulation results and the experimental measurements as reported in [9].

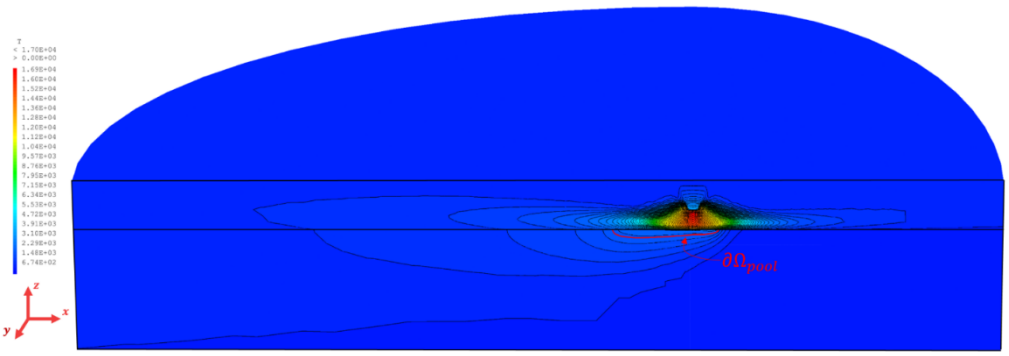

Figure 7. Temperature field of simulated case of the weld displacement configuration

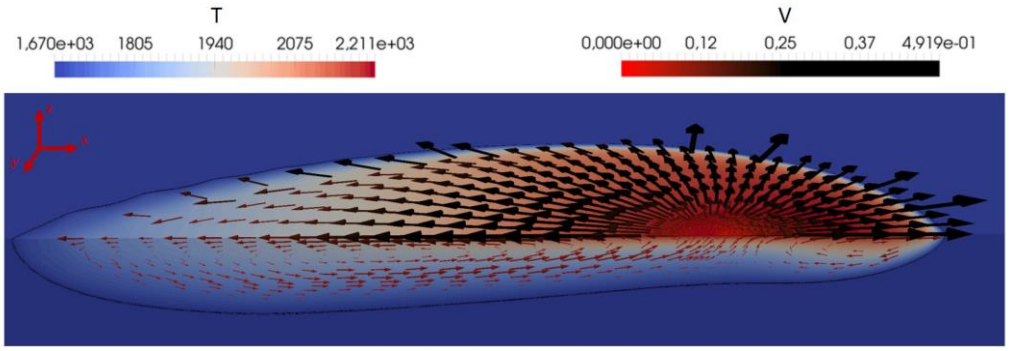

Figure 8. A closeup of the pool temperature and velocity fields

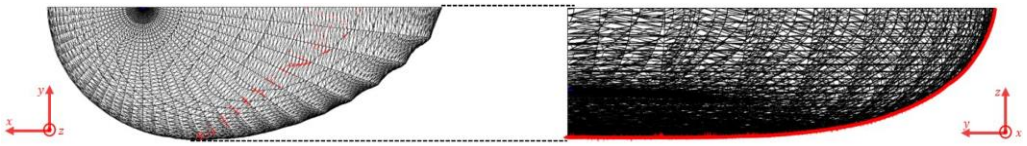

Figure 9. Calculated maximum depth isocontour on the simulated pool geometry

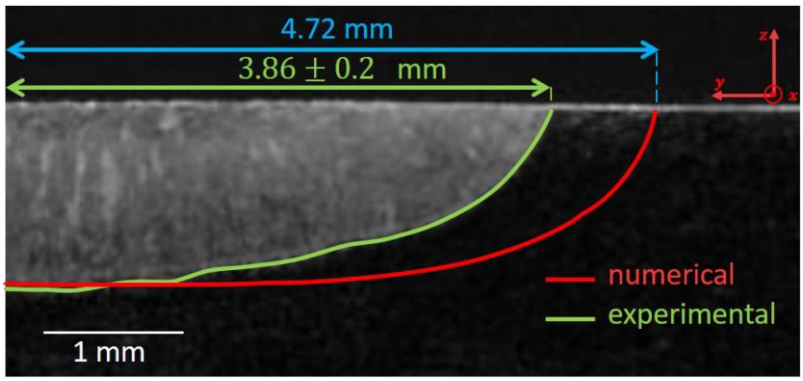

Figure 10. Comparison of numerical maximum depth isocontour to the experimental macrographic cross section from [12]

4.2 Comparison to experimental measurements

To compare the calculated pool geometry to the experimental macrographic image reported by Koudadje [9], the appropriate calculated pool geometry projection must be considered. In fact, referring to Figure 8, the pool geometry is not deepest where it is widest; furthermore, the pool floor exhibits multiple inflection points. Thus, calculating the equivalent macrographic slice from a stationary pool model requires that the maximum depth isocontour be calculated as a function of the x and y axes. The calculated maximum depth isocontour for the pool geometry is presented in Figure 9 and is represented by the red points and contour on the mesh of the pool geometry. Using the equivalent numerical macrographic projection the results are compared to the experimental cross section in Figure 10. Indeed, the calculated pool depth agrees with the experimentally measured depth; however, the calculated pool width is 22%

larger than the experimental one. Although the simulated welding configuration yields a pool profile that is of the same order of magnitude as the experimental cross section, a discussion of the potential sources of discrepancy can be found in [1].

5 Conclusion

In this paper, we present the work done on the conjugate heat transfer module of our 3D unified TIG welding model, where a novel interface coupling method was mathematically described. The quasi-monolithic algorithm, which is based on an asymmetric thermal constraint, conserves energy at the arc-workpiece interface; however, the asymmetry renders thermal continuity weakly imposed. This method is shown to be at least stable within the scope of our application, even for 3D configurations. Furthermore, certain simulation results using the full model (as adapted from [1]) are shown to be comparable to an experimental case chosen from the literature. The authors encourage further research into non-associated relations, and themselves will publish future works on this broad topic.

6 References

[1] C. Nahed, "Magneto-thermo-hydrodynamic modelling of TIG welding: a 3D unified coupling of the arc-plasma and the weld pool", Doctoral dissertation, Aix-Marseille, 2021.

[2] C. Nahed, S. Gounand, and M. Medale, "A numerical study of the effects of cathode geometry on tungsten inert gas type electric arcs," *International Journal of Heat and Mass Transfer*, vol. 182, p. 121923, Jan. 2022.

[3] M. A. Ramírez, "Mathematical modeling of D.C. electric arc furnace operations," dspace.mit.edu, 2000.

[4] M. Brochard, "Modèle couplé cathode-plasma-pièce en vue de la simulation du procédé de soudage à l'arc TIG," theses.fr, Jan. 01, 2009.

[5] Giles, M.B. (1997), Stability analysis of numerical interface conditions in fluid–structure thermal analysis. Int. J. Numer. Meth. Fluids, 25: 421-436.

[6] P. Causin, J. F. Gerbeau, and F. Nobile, "Added-mass effect in the design of partitioned algorithms for fluid–structure problems," Computer Methods in Applied Mechanics and Engineering, vol. 194, no. 42–44, pp. 4506–4527, Oct. 2005.

[7] A. Baumard, D. Ayrault, O. Fandeur, C. Bordreuil, and F. Deschaux-Beaume, "Numerical prediction of grain structure formation during laser powder bed fusion of 316 L stainless steel," Materials & Design, vol. 199, p. 109434, Feb. 2021.

[8] B. P. Renaudie, "Effect of welding on stress relaxation cracking in AISI 316L(N) austenitic stainless steel", Doctoral dissertation, Mines-Paris-PSL, 2023.

[9] K. Koudadge, " Experimental study and numerical modelling of weld pool during GTA welding of steels ", Doctoral dissertation, Aix-Marseille, 2013.

[10] F. Lago, J. J. Gonzalez, P. Freton, and A. Gleizes, “A numerical modelling of an electric arc and its interaction with the anode: Part I. The two-dimensional model,” Journal of Physics D: Applied Physics, vol. 37, no. 6, pp. 883–897, Feb. 2004.

[11] V. R. Voller, M. Cross, and N. C. Markatos, “An enthalpy method for convection/diffusion phase change,” International Journal for Numerical Methods in Engineering, vol. 24, no. 1, pp. 271–284, Jan. 1987.

[12] M. C. Nguyen, “Modélisation et simulation multiphysique du bain de fusion en soudage à l’arc TIG”, Doctoral dissertation, Aix-Marseille, 2015.

[13] J. N. Reddy, Introduction to the finite element method. 2018.

[14] P. Verpeaux, C. Berthinier, A. Millard, “Utilisation de relations non-associées en mécanique des structures,” 15eme Colloque National en Calcul des Structures, 2022.

[15] C. Lanczos, The variational principles of mechanics. New York: Dover Publications, Post, 2005.